The impact of gravity wave drag on mesospheric analyses of the 2006 stratospheric major warming

Shuzhan Ren,[1] Saroja Polavarapu,[2] Stephen R. Beagley,[3] Yulia Nezlin,[1] and Yves J. Rochon[2]

[1]   The 2006 Arctic stratospheric sudden warming was an unusual event in which the stratopause disappeared after the peak of the warming, only to reform at very high altitudes above 75 km. The stratopause then descended during February and March 2006, returning to climatological values. This event, which coupled the troposphere, stratosphere, and mesosphere, has been used to assess the quality of the upper stratospheric and mesospheric analyses produced with the Canadian Middle Atmosphere Model's data assimilation system. By comparing with simulations in which Sounding of the Atmosphere Using Broadband Emission Radiometry temperatures were assimilated, mesospheric analyses obtained without assimilating any observations above 45 km were shown to capture the timing and amplitude of the elevated stratopause event. Mesospheric analyses of temperature and winds were sensitive to the use of a nonorographic gravity wave drag scheme, but this sensitivity was reduced when mesospheric temperatures were assimilated. Moreover, a realistic nonorographic gravity wave drag can somewhat compensate for the lack of mesospheric measurements. On the other hand, the descent of mesospheric NO_x after the peak of the stratospheric warming was found to be sensitive to the presence of nonorographic gravity wave drag even when mesospheric temperatures were assimilated, suggesting that eddy forcing is not fully constrained by mesospheric observations in our data assimilation system.

Citation: Ren, S., S. Polavarapu, S. R. Beagley, Y. Nezlin, and Y. J. Rochon (2011), The impact of gravity wave drag on mesospheric analyses of the 2006 stratospheric major warming, *J. Geophys. Res.*, *116*, D19116, doi:10.1029/2011JD015943.

1.   Introduction

[2]   Many operational assimilation systems are now capable of resolving the entire stratosphere and even the lower mesosphere. The European Centre for Medium-Range Weather Forecasts (ECMWF) raised the lid of its operational model in February 2006 to 0.01 hPa, the Global Modeling and Assimilation Office (GMAO) did so in January 2004 and the Met Office moved to a lid of 80 km in November 2009. A model lid height of 0.01 hPa (roughly 80 km) permits a sponge layer above 1 hPa, the climatological stratopause height, and thus a good depiction of the upper stratosphere also. Given the availability of operational analyses for process studies, and the availability of measurements of the upper stratosphere–lower mesosphere (USLM) region from a variety of sources (such as the Sounding of the Atmosphere Using Broadband Emission Radiometry (SABER) [*Russell et al.*, 1999], the Microwave Limb Sounder (MLS) [*Waters et al.*, 2006], Odin Sub Millimeter Radiometer (SMR) [*Murtagh et al.*, 2002], Atmospheric Chemistry Experiment Fourier Transform Spectrometer (ACE-FTS) [*Bernath et al.*, 2005] and mesospheric radars [e.g., *Hoffmann et al.*, 2007] and lidars [e.g., *Thurairajah et al.*, 2010]) it is natural to consider the quality of analyses in this region.

[3]   Stratospheric sudden warmings (SSWs) are perhaps the most dynamic stratospheric events seen in winter polar regions. By definition, a major SSW involves a dramatic warming of polar temperatures (by 40–60K) over one week, temporarily reversing the meridional temperature gradient and changing the direction of the polar night jet at 60°N from westerly to easterly [*Andrews et al.*, 1987]. A cooling of the mesosphere may also occur in conjunction with the warming of the stratosphere as first noted by *Labitzke* [1972]. Since these events are driven by upward propagating planetary waves from the troposphere [*Matsuno*, 1971], they offer an opportunity to study the coupling of the troposphere, stratosphere and even the mesosphere.

[4]   While the stratopause drops in altitude during a typical SSW, an unusual phenomenon has been observed more recently in which the stratopause temporarily disappears after a major SSW, and reforms at very high altitudes (above 75 km). Examples of such events occurred in 2004, 2006 and 2009 [*Randall et al.*, 2006; *Manney et al.*, 2009a, 2009b; *Orsolini et al.*, 2010; *Thurairajah et al.*, 2010]. During such events, the stratopause descends from around 75 km to its

---

[1]Department of Physics, University of Toronto, Toronto, Ontario, Canada.
[2]Environment Canada, Toronto, Ontario, Canada.
[3]Department of Earth and Space Science and Engineering, York University, Toronto, Ontario, Canada.

climatological height of 1 hPa (63 km) over 1.5–2 months [*Orsolini et al.*, 2010]. As a result, trace species from the upper atmosphere can be isolated in a strengthening polar vortex and brought to stratospheric levels while shielded from sunlight. For example, descent of NO_x (=NO + NO_2) [*Randall et al.*, 2006], CO [*Manney et al.*, 2009a, 2009b], and H_2O [*Orsolini et al.*, 2010; *Manney et al.*, 2009b] was observed during the 2006 event. Indeed, *Randall et al.* [2006] and *Hauchecorne et al.* [2007] argue that stratospheric variability is more important for understanding the presence of NO_x at stratospheric levels than knowledge of energetic particle precipitation events alone. In addition to the relevance for constituent distributions, the dramatic changes in the stratosphere and mesosphere are a result of, and have implications for wave activity. *Coy et al.* [2009] suggest that wave reflection from a subtropical wave breaking event in the troposphere was a crucial precursor of the 2006 SSW. *Siskind et al.* [2007] found that the suppression of orographic gravity wave drag (GWD) was important for capturing the formation of the high stratopause and observational evidence confirms this view [*Wright et al.*, 2010]. *Siskind et al.* [2010] found that nonorographic gravity wave drag was important when the stratopause was elevated. As well, planetary wave activity decreased in the upper stratosphere after the SSW when the stratopause disappears [*Siskind et al.*, 2007, 2010; *Manney et al.*, 2008]. After the SSW, during the slow descent of the high stratopause over several weeks, enhanced gravity wave activity was observed [*Hoffmann et al.*, 2007]. The role of waves (resolved or parameterized) in the creation and evolution of the elevated stratopause in 2006 was discussed by *Siskind et al.* [2010], while *Limpasuvan et al.* [2011] performed a similar evaluation but for a simulated event using a climate model with a 145 km lid.

[5] The 2006 SSW event, being well observed, offers an opportunity to examine the performance of assimilation systems during an event in which the troposphere, stratosphere and mesosphere were strongly coupled. Despite the model lid heights of roughly 80 km, *Manney et al.* [2008] found that operational assimilation systems (from ECMWF and GMAO) did not capture well the timing, amplitude and height of the stratopause disappearance and reformation. This is perhaps not too surprising since the stratopause reforms at 75 km: too close to the model tops to be well depicted. At the same time, research assimilation systems such as the Canadian Middle Atmosphere Model Data Assimilation System (CMAM-DAS) [*Polavarapu et al.*, 2005; *Sankey et al.*, 2007] and the Navy Operational Global Atmospheric Prediction System Advanced Level Physics High Altitude (NOGAPS-ALPHA) with model lids near 95 km were able to better capture the stratopause behavior [see *Polavarapu et al.*, 2008; *Siskind et al.*, 2010; *Hoppel et al.*, 2008; this study]. The NOGAPS-ALPHA system assimilated both SABER and MLS temperatures and thus agreement with those observations was quite good [*Siskind et al.*, 2010; *Hoppel et al.*, 2008] but not surprising. However, CMAM-DAS assimilated no observations above 1 hPa, yet also agrees well with SABER and MLS temperatures. Thus, an interesting question is why? *Nezlin et al.* [2009a] have shown that observations from the stratosphere and troposphere can impact large scales in the mesosphere. This can occur through upward propagating resolved waves

[*Sankey et al.*, 2007] or through parameterized waves [*Ren et al.*, 2008]. Thus during a SSW which is forced by upward propagating waves, observations of the troposphere and stratosphere may be sufficient to describe the large-scale mesospheric response, if waves can be depicted well by the model. Since gravity waves played a role in the 2006 SSW [*Siskind et al.*, 2010], the quality of their depiction (whether through resolved or parameterized waves) in models should be important for capturing stratopause evolution. On the other hand, stratopause evolution can also be captured by assimilating mesospheric temperatures [*Siskind et al.*, 2010; *Hoppel et al.*, 2008]. Thus, the goal of this work is to examine the interplay between observations and gravity wave drag in the context of a data assimilation system. We shall demonstrate that mesospheric observations are not needed to capture some aspects of the mesospheric evolution during the 2006 SSW. On the other hand, even when mesospheric observations are assimilated, some aspects of mesospheric analyses are still sensitive to GWD.

[6] The article is organized as follows. In section 2, the CMAM-DAS and the numerical experiments are described. In section 3, we demonstrate that the CMAM-DAS depicts well the stratopause evolution during the 2006 SSW, without the benefit of observations above 45 km. Then in section 4, we examine the role that nonorographic GWD played in the quality of the simulations. A summary and conclusions are presented in section 5.

2. The CMAM-DAS Assimilation Cycles

[7] Since the CMAM and its data assimilation system were described by *Polavarapu et al.* [2005] (hereinafter P05), we focus here on differences from that system.

2.1. The CMAM-DAS

[8] The CMAM is a complex interactive chemistry, radiation and dynamics model which extends from the ground to the mesopause. It is based upon the Canadian Climate Centre's General Circulation Model (GCM) whose dynamical and physical core is described by *Scinocca et al.* [2008]. The version used as the basis for the CMAM-DAS is described in the SPARC CCMVal report [*Eyring et al.*, 2010]. CMAM is a spectral model and here uses a triangular truncation of T47 with a Gaussian collocation grid of 96 × 48 points (a grid spacing equivalent of approximately 3.75° for the physics) and a 7.5 min time step. Here 71 vertical levels extending from the ground to approximately 95 km are used, with a model lid pressure of 0.000575 Pa. Tracers are spectrally advected with many chemical species transported as families, while water is a "hybrid" [*Boer*, 1995] advected field.

[9] The current version of CMAM on which this series of experiments is based has changed in a number of aspects compared to that described in P05. Most importantly the parameterized GWD schemes for both the orographic and nonorographic waves have been changed to those described by *Scinocca et al.* [2008]. The stratospheric chemistry has remained largely unchanged [*de Grandpré et al.*, 2000] but active chemistry in the troposphere has been included, where before chemical tracers were inert between the surface and 400 hPa. The chemistry of the troposphere includes a description of methane-NO_x chemistry and associated processes
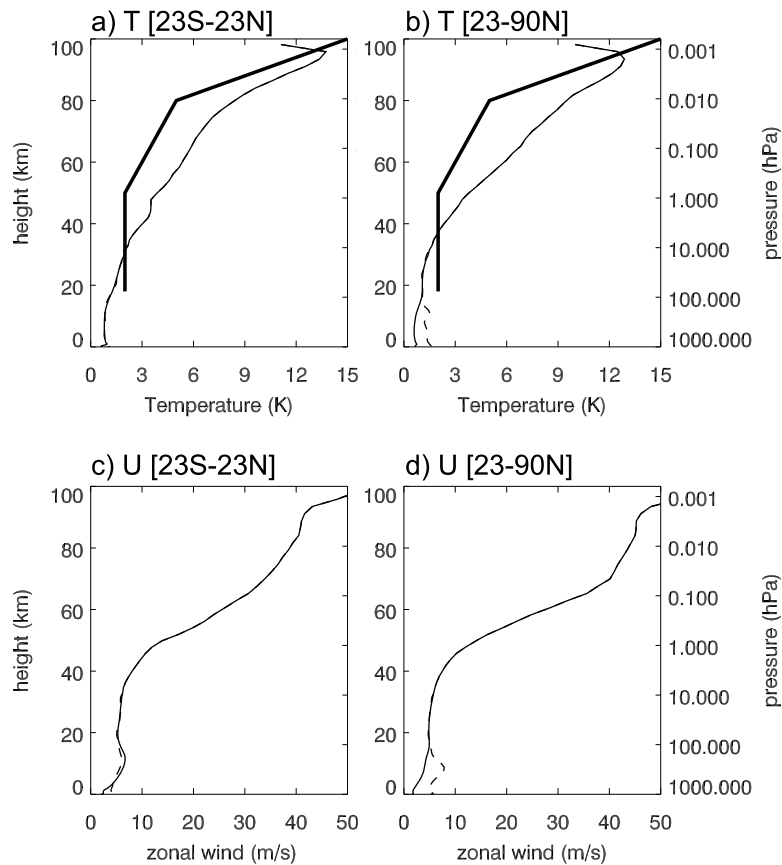
Figure 1. Forecast and observation error standard deviations for (top) temperature and (bottom) zonal wind. Values are averaged over tropics (a, c) [23°S, 23°N] and (b, d) [23°N, 90°N]. Observation error standard deviations for Sounding of the Atmosphere Using Broadband Emission Radiometry (SABER) (bold lines) and forecast error standard deviations for the old (dashed lines) and new (solid lines) versions are shown. The pressure axis is approximate and was obtained assuming a constant scale height of 7 km and a reference value of 1000 hPa. The same approximation is used in Figures 2, 8–10, and 16.

such as emissions of CO and NO_x, wet and dry deposition and the effects of clouds on photolysis rates. The version used here was a developmental version and did not include the emissions of NO_x from lightning, which will lead to a low bias in tropospheric ozone over large parts of the globe, particularly in the tropics. The CMAM is also now run in a transient mode with ocean and chemical forcings provided for the years under analysis, compared to the time-slice approach in P05.

[10] As in P05, the assimilation scheme is still 3D-Var but now observations are compared to model background fields at the closest hour during the 6 h assimilation window. Thus, a first guess at appropriate time (FGAT) scheme is used, as by *Simmons* [2000] (available from http://www.ecmwf.int/publications/library/ecpublications/_pdf/seminar/2000/). A maximum time mismatch error of 30 min is possible now, compared to the 3 h error possible in P05. The digital filter used in P05 was replaced by an incremental analysis updating (IAU) scheme [*Bloom et al.*, 1996; *Polavarapu et al.*, 2004] with constant coefficients. As noted by *Sankey et al.* [2007], this scheme provides global mean mesopause temperatures and mesospheric tides that are in better agreement with observations than the other schemes assessed. The standard set of observations were assimilated from

conventional platforms as well as wind profilers, atmospheric motion vectors and radiance observations (Advanced Microwave Sounding Unit (AMSU)-A ch. 3–13, AMSU-B ch. 2–5, Microwave Humidity Sounder (MHS)). AMSU-B and MHS are new observation types (not used in P05) that are sensitive to temperature and moisture in the troposphere. (Advanced Microwave Sounding Unit-A channels 11–13 from NOAA-15 and 16 were used, but these channels were inadvertently omitted from NOAA 18 and AQUA.)

[11] Background error covariances in P05 were computed using 6 h time differences of states from a climate model run. This method has been referred to as the Canadian Quick Covariance method [*Jackson et al.*, 2008]. Here, tropospheric variances were updated using an ensemble perturbation approach as of *Buehner* [2005], except that only observations were perturbed and the observations were simulated from a CMAM free run as by *Nezlin et al.* [2009a, 2009b]. (The CMAM variability is large enough that additional background error perturbation was not necessary.) The variances so derived are a function of observation errors and distribution (unlike those of P05). Following an impact assessment using radiosonde observations, only variances below roughly 100 hPa were updated. The new variances were matched with old variances using repeated applications of
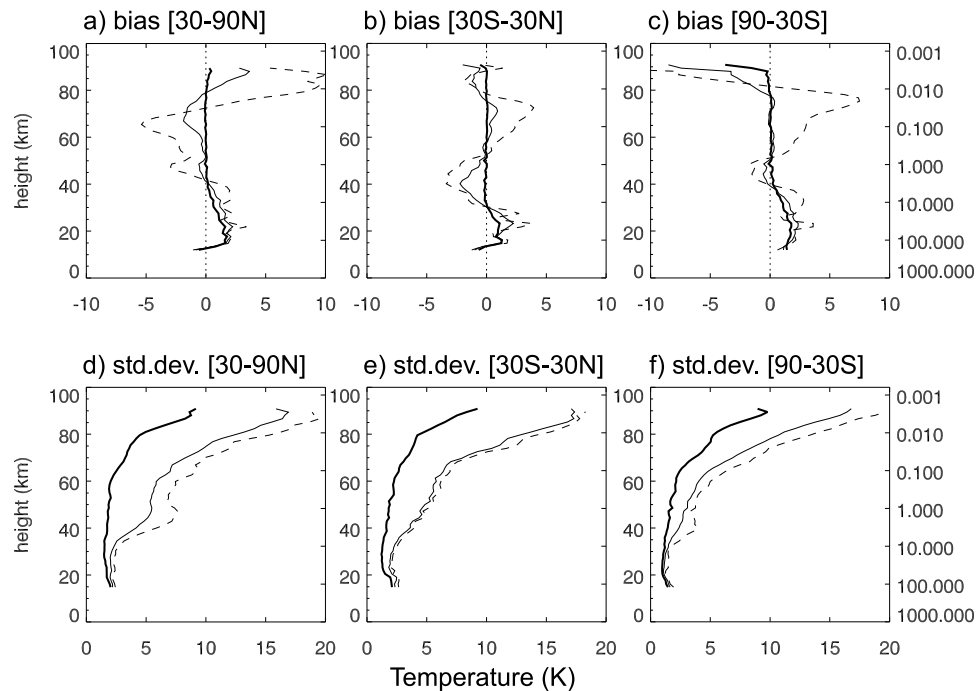
Figure 2. SABER minus assimilated temperatures averaged over various latitude bands. Statistics were computed for January 2006 using 123 samples. SABER minus 6 h forecast fields are shown for the CONTROL assimilation cycle (dashed lines) and SABER assimilation cycle (solid lines). The bold lines show SABER minus analyses from the SABER assimilation cycle. Biases are shown for the (a) Northern Hemisphere, (b) tropics, and (c) Southern Hemisphere, while standard deviations are shown for the (d) Northern Hemisphere, (e) tropics, and (f) Southern Hemisphere.

a 1-2-1 smoother in the vertical overlap region. Figure 1 shows an example of the old (dashed curves) and new (solid curves) standard deviations for the Northern Hemisphere high-latitude band. The main impact is a reduction of standard deviation in the midlatitude jet region since the 6 h difference method used by P05 overestimates them there. As in P05, no coupling between mass and wind increments is permitted in the mesosphere and correlations do not spread increments from the stratosphere into the mesosphere. Since the balance constraint on increments in our system is not scale dependent, it must apply to all scales or to none. Yet neither choice is entirely correct since divergent motions dominate the mesospheric energy spectrum at intermediate and smaller scales, but balance is relevant at the largest scales [*Koshyk et al.*, 1999].

2.2. The Assimilation Experiments

[12] Assimilation experiments were run in order to simulate the major stratospheric sudden warming of 2005–6. The CONTROL assimilation cycle started on 1 December 2005 and was continued until 1 April 2006. In order to compare this CONTROL cycle with mesospheric observations, a second cycle was run in which SABER temperature observations were assimilated (for the same dates). SABER version 1.07 retrieved temperatures were used between roughly 20–100 km. SABER views on the anti-Sun side of the spacecraft resulting in asymmetric global coverage during any 60 day period. From 1 December 2005 to 13 January 2006 it was in the south-looking mode with latitudinal cov-

erage from and from 52°N–83°S. During 13 January 2006 to 17 March 2006 it was in north-looking mode which has a latitude range of 52°S–83°N. Observation error standard deviations were initially chosen to match those found in the work of *Remsberg et al.* [2008, Figure 6]. After one assimilation cycle observation errors were modified so that they did not exceed the sum of observation and background error variances, thus producing the values shown in Figure 1. Since no other mesospheric observations were assimilated, no bias corrections of SABER temperatures were done. A gross quality control check was applied in which observations beyond 4σ (background plus observation error standard deviation) from the background were rejected. Variational quality control was also used, as for all other observations.

[13] Figure 2 shows that when SABER observations are assimilated, analysis errors (heavy solid curves) are reasonably small in terms of both mean (top row) and standard deviation (bottom row). The bias of the 6 h forecast errors for the CONTROL cycle (dashed curves) is much larger than that of the SABER cycle (solid curves). Assimilating SABER helps to reduce the forecast bias though some bias remains below 40 km. Since this height region includes other observations from AMSU-A (channels 12–13), the bias may be due to a relative bias between these two types of observations, or to the bias correction procedure applied for AMSU-A channels. Since *Remsberg et al.* [2008] found that SABER temperatures have a warm (cold) bias of 1–3 K in the lower (upper) stratosphere relative to other measurements, our results are consistent with a bias of SABER with
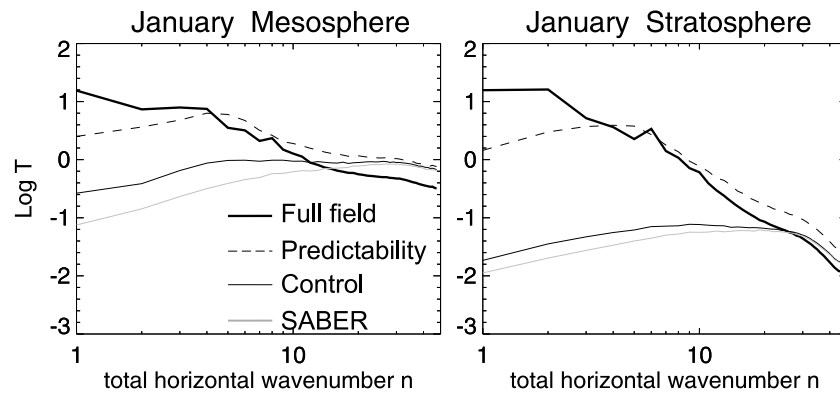
Figure 3. Log_{10} of temperature spectra averaged vertically and in time. The bold lines represent the full state of the Canadian Middle Atmosphere Model (CMAM) (computed from a reference simulation), while the dashed lines refer to the predictability errors of the CMAM. Six hour temperature forecast error spectra are shown when no mesospheric observations are assimilated (solid curves) and when SABER temperatures are assimilated (shaded curves). Spectra are averaged (left) over all mesospheric model levels and (right) over all stratospheric model levels. They are also averaged in time after errors have saturated, using the last 10 days of the assimilation cycles.

respect to AMSU-A. The standard deviations of analysis errors are around 2–3 K for most of the troposphere and stratosphere (bottom row, heavy solid curves). Standard deviations of 6 h forecast errors of the SABER cycle (solid curves) increase rapidly with height above 30 km and are much larger than those for analysis errors. *Hoppel et al.* [2008] have only a 6 K standard deviation in the mesosphere whereas 6–18 K is seen for 60–90 km in the Northern Hemisphere in Figure 2d. There are a few possible reasons for the larger values seen here. First, *Hoppel et al.* [2008] used much larger values of observation errors (ranging from 9 to 15 K from 1 to 0.01 hPa). On the basis of experience, fitting observations more closely (e.g., smaller observation error standard deviations) generally leads to larger 6 h forecast errors. Second, differences in correlation widths (horizontally and vertically) will result in a different spatial influence of observations. Third, *Hoppel et al.* [2008] use geostrophic balance to couple mass and wind increments in the extratropical mesosphere, whereas we used none here. Finally, the variability of the underlying models is undoubtedly different. CMAM variability is known to be large in the mesosphere [e.g., *Nezlin et al.*, 2009a, 2009b]. In Figure 2, the benefit of assimilating SABER on 6 h forecast standard deviations is greatest in the Northern Hemisphere. For example, an improvement of over 5 K is seen at 70 km (compare solid and dashed curves in Figure 2d). In the Southern Hemisphere, observations were available only to 52°S during January 2006 likely limiting their impact. The reason for the modest impact of SABER observations in the tropics (Figure 2e) is unclear but is consistent with results of assimilation experiments with simulated SABER observations (in which no model or observation error biases were present) (not shown).

[14] *Nezlin et al.* [2009a] showed that mesospheric analysis error spectra in the case of a perfect model (meaning observations were generated with the same model used for assimilation) and observations errors consistent with specified error variances were not reduced below predictability levels for wave numbers above 10 when only observations

below the mesosphere were assimilated. Figure 3 shows error spectra from a similar experiment in which SABER temperatures were also assimilated. While *Nezlin et al.* [2009a] demonstrated that observations below 1 hPa helped improved large scales in the mesosphere, Figure 3 shows that the largest scales (below wave number 10) are further improved when SABER temperatures are assimilated. This corresponds to an extension of predictable scales from 3 to 5 days in the mesosphere (not shown). For small length scales, errors approach the predictability limit (obtained by computing the level of saturation of differences between simulations from two different initial conditions when no assimilation is performed) in the mesosphere. In the stratosphere, errors are 2–3 orders of magnitude smaller than the full field itself (heavy solid curve) for wave numbers below 10 and all scales are predictable. Thus SABER temperatures mainly improve large scales in the middle atmosphere in the CMAM-DAS. The fact that wave numbers higher than 10 are not expected to be improved by assimilating SABER temperatures in the CMAM-DAS suggests that the large variances of observation minus 6 h forecast differences seen in Figure 2 reflect the lack of observability of mesospheric scales higher than wave number 10 for the CMAM-DAS.

[15] In order to diagnose the role of gravity wave drag (GWD) on the assimilation fields, the CONTROL and SABER cycles were rerun during January 2006 with no nonorographic GWD scheme. The orographic GWD scheme was still used however. These cycles (CONTROL–no GWD and SABER–no GWD) were started on 1 January 2006 and run

Table 1. Configuration of the Assimilation Experiments

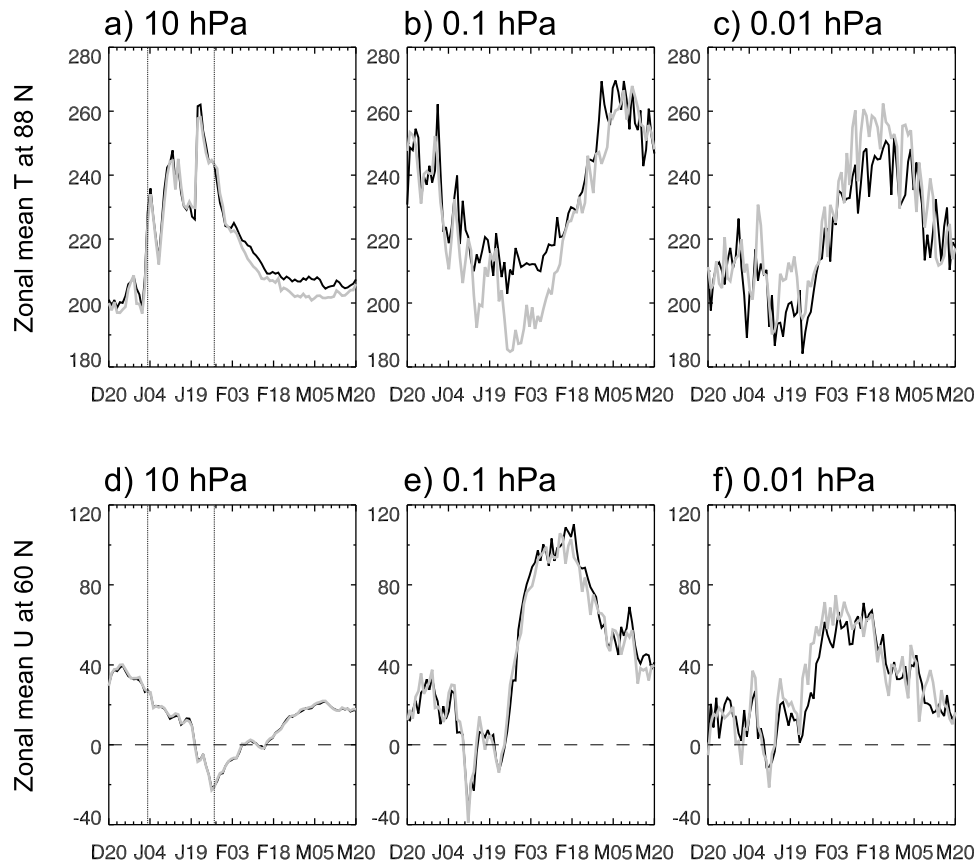| Experiment Name	SABER Temperatures Assimilated	Orographic GWD Used	Nonorographic GWD Used
CONTROL	no	yes	yes
CONTROL–no GWD	no	yes	no
SABER	yes	yes	yes
SABER–no GWD	yes	yes	no

Figure 4. Time series of temperature at 88°N and zonal mean wind at 60°N from 20 December 2005 to 20 March 2006 for the CONTROL (solid curves) and SABER (shaded curves) assimilation cycles. (top) Temperature and (bottom) zonal mean wind are shown for (a, d) 10 hPa, (b, e) 0.1 hPa, and (c, f) 0.01 hPa. Vertical bars indicate the center dates for two of the time periods used in Figures 8 and 9, namely, 3 and 27 January 2006.

until 15 February 2006. The names and configuration of the 4 cycles discussed in this work are presented in Table 1.

3. Stratospheric and Mesospheric Evolution During 2005–2006

[16] In this section, we demonstrate that the CONTROL assimilation cycle (in which no observations above 1 hPa are assimilated) depicts well the mesospheric evolution of the 2006 SSW by comparing it to the SABER assimilation cycle.

3.1. Physical Description of the 2006 SSW

[17] Figure 4 shows time series of temperature at the North Pole (top row) and zonal mean wind at 60°N (Figures 4d–4f) at three heights. The temperature at 10 hPa reaches a maximum on 26 January (Figure 4a) after a few minor warmings in early January. In conjunction with the stratospheric warmings, mesospheric coolings are seen (Figures 4b and 4c). After the peak of the SSW (defined as 27 January when the maximum easterly wind at 10 hPa is seen), stratospheric and lower mesospheric temperatures gradually return to their prewarming values (Figures 4a and 4b). However, in the upper mesosphere (Figure 4c), the North

Pole temperature increases dramatically, reaching 250–40 K more than its prewarming value. This peak in mesospheric warming occurs at the same time that an elevated stratopause forms at 75 km (shown later), slowly descending through February and March. A wind reversal occurs at the peak of the SSW (on 27 January) in both stratosphere and mesosphere (Figures 4d–4f). After the peak, stratospheric winds return to westerly but their magnitude is just half of the prewarming value (Figure 4d). In the mesosphere, however, a strong polar vortex reforms and the maximum speed is more than two times larger than seen before the SSW (Figures 4e and 4f).

[18] Both CONTROL and SABER cycles capture the features of temperature and zonal wind evolution in the middle atmosphere. At the standard 10 hPa level, the largest differences in temperature occur in February and March (Figure 4a). At this height both cycles use other satellite data and SABER data is about 20% of the total. At 0.1 and 0.01 hPa, larger temperature differences are seen, with the SABER cycle providing over 20 K lower temperatures on 25 January (Figure 4b). At these heights SABER is the only data source. Differences in zonal mean zonal wind seem smaller than temperature differences because zonal means
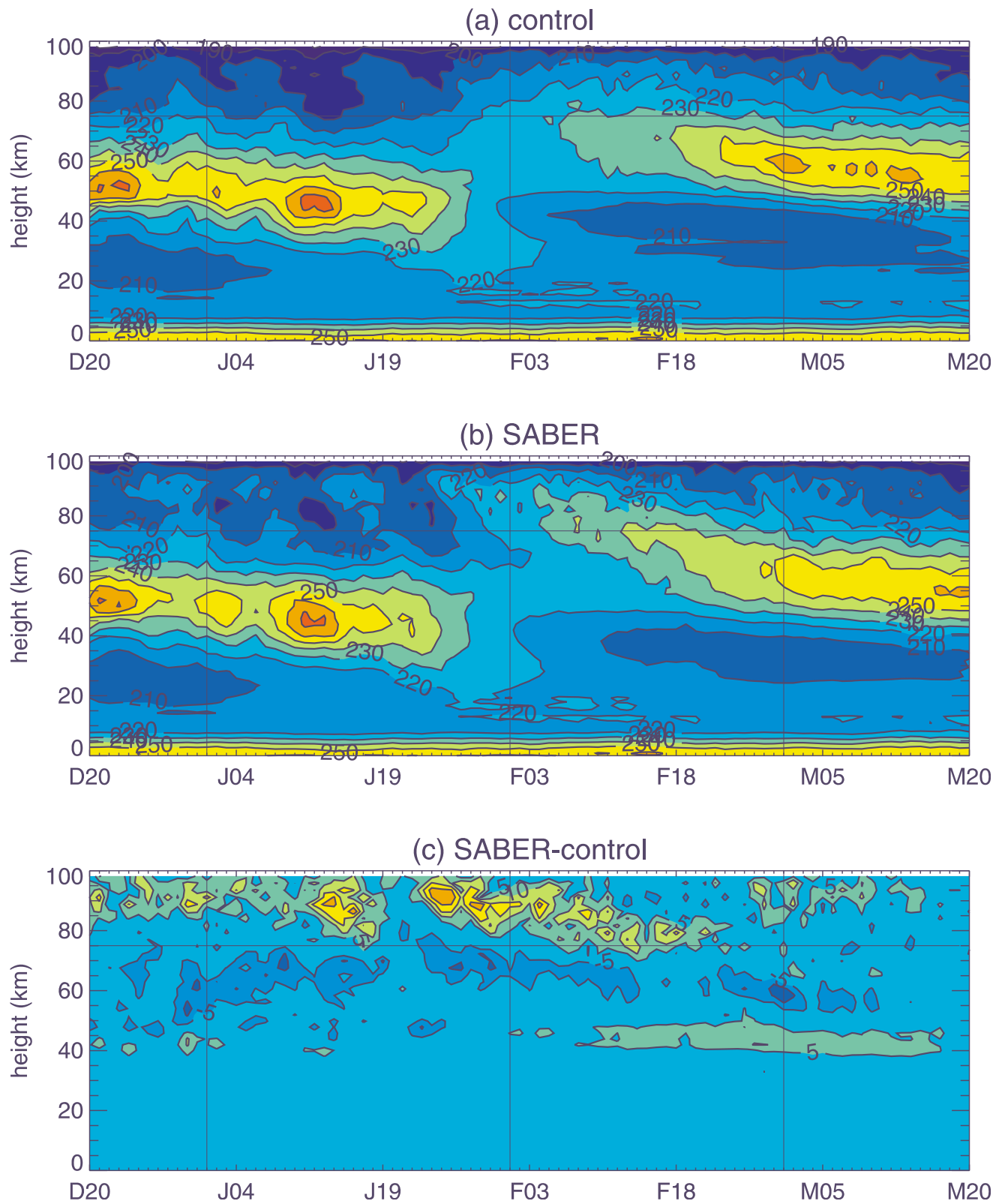
Figure 5. Time series of zonal mean temperature fields (K) at 70°N as a function of height for (a) the CONTROL cycle, (b) the SABER cycle, and (c) the difference between the two cycles. The horizontal axis is time starting on 20 December 2005 and ending on 20 March 2006, with ticks every day. Contour intervals are 10 K (Figures 5a and 5b) and 5 K (Figure 5c) with the zero contour omitted. Vertical lines indicate the first of each month.
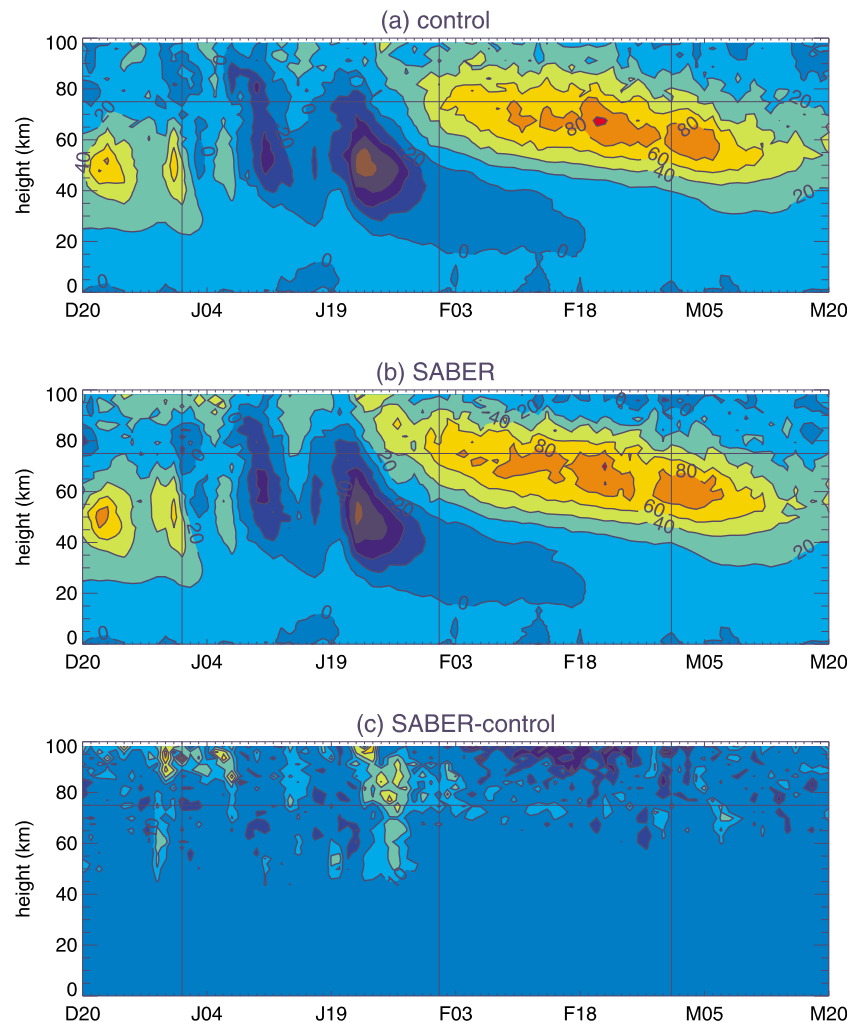
Figure 6. Same as Figure 5, but for zonal mean zonal wind fields at 70°N. Contours are 10 m/s. In Figure 6c, the zero contour is omitted.

are shown in (Figures 4d–4f) whereas a single time series is shown in Figures 4a–4c.

[19] Time series of zonal mean temperature are compared in Figure 5. The elevated stratopause and the timing of the disappearance and reemergence of the stratopause are captured by the CONTROL cycle. However, the SABER cycle produces a stratopause of over 80 km in early February while a lower value of 75 km is seen in the CONTROL. (The SABER observed value of 0.005 hPa would be in the CMAM nonzonal sponge layer.) *Orsolini et al.* [2010] find a stratopause height of 75 km using ODIN/SMR, as does *Manney et al.* [2008] from MLS and SABER observations. *Manney et al.* [2008] also note that neither GMAO nor ECMWF stratopause analyses reach this height in early February. Through the assimilation of MLS and SABER temperatures, the NOGAPS-ALPHA system obtains an 80 km stratopause height [*Siskind et al.*, 2010], consistent with the SABER observed value of 0.005 hPa. Figure 6 compares the zonal mean zonal wind time series and again reveals that the CONTROL cycle captures the timing and magnitude of the zonal wind reversals as well as the reformation of the strong polar jet after the peak of the SSW. Interestingly, the difference between the two cycles is largest during the

peak of the SSW (around 27 January). Differences between the two cycles are notably smaller in the mesosphere below 75 km during February and March.

[20] Figure 7 demonstrates that the CONTROL cycle, like NOGAPS-ALPHA, can also produce a stratopause height of 75 km at this time, even without the benefit of assimilating mesospheric observations. The stratopause was defined as the local temperature maximum of a profile and is thus sensitive to noise in the profiles due to high-frequency signals. The difference in the timing of the jump in stratopause height is not important because the computation of stratopause height is very sensitive to noise when the atmosphere is essentially isothermal (as it was after the peak of the SSW in late January). The slow descent of the stratopause during February and March is also captured by both assimilation cycles. The reduction in stratopause height of 20–30 km seen in Figure 6 is consistent with that seen in MLS observations by *Manney et al.* [2008]. The rate of stratopause descent is 30 km in 56 days or about 6 mm/s which is consistent with that seen by *Randall et al.* [2006, Figure 1], *Manney et al.* [2008, Figure 1], and *Manney et al.* [2009a, Figure 1c].
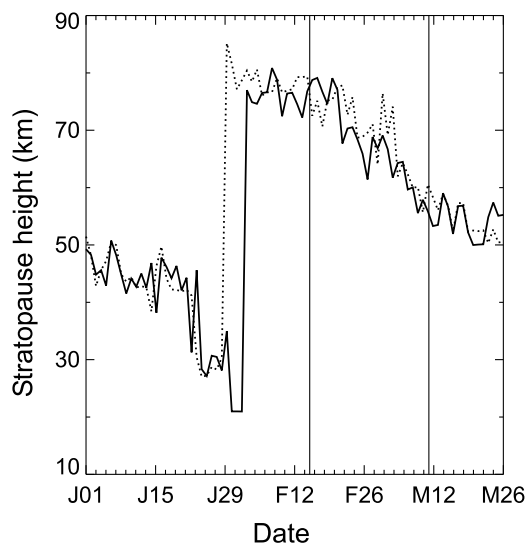
Figure 7. Evolution of stratopause height at 88°N in the CONTROL (solid curve) and SABER (dotted curve) assimilation cycles. The horizontal axis is time starting on 1 January and ending on 26 March, with ticks every 2 days. The vertical lines indicate the later two time periods used in Figures 8 and 9, namely, 15 February 2006 and 11 March 2006.

3.2. Analysis of Wave Activity

[21] As the middle atmospheric circulation in winter is largely wave driven [e.g., *Shepherd*, 2008], it is useful to assess the contribution of various wave sources to the forcing of the zonal mean flow. For this reason, we compute the residual vertical velocity (or $\overline{w}*$) implied by downward control [*Haynes et al.*, 1991] for resolved and parameterized waves (see the appendix for details). All computations were done offline (not as part of the assimilation cycle but after it) using analyzed wind and temperature fields. In climate simulations, an offline computation of GWD may not reflect the forcing obtained during the simulation. This is because of the interaction between resolved and parameterized wave forcings [*Alexander et al.*, 2010]. Specifically, the

parameterized wave forcing affects the zonal mean flow, which affects the forcing by resolved waves. However, in an assimilation cycle where observations constrain the troposphere and stratosphere to observed values, the resolved wave forcing (at least on large scales) is known. Thus the parameterized wave forcing can be determined offline since no feedback between resolved and unresolved waves will occur. Strictly speaking, the downward control implied residual vertical velocity is valid in the steady state limit whereas SSWs are highly dynamic events. Thus, our results should be viewed qualitatively rather than quantitatively. Furthermore, the diagnostic is mainly used to compare results from the various assimilation cycles for which the diagnostic is similarly applied. Here the computations were done over 5 days (17 snapshots) but the computations of residual vertical velocity ($\overline{w}*$) were found to be robust in that quantitatively similar results were obtained for averaging periods between 3 and 6 days.

[22] Figure 8 shows the zonal mean zonal wind profiles at 60°N averaged over 4 different time periods for the CONTROL (Figure 8a) and SABER (Figure 8b) cycles. The time periods are chosen to represent different stages of the SSW and elevated stratopause events. The dates 1–5 January 2006 represent the typical winter conditions occurring before the SSW; 25–29 January represent the peak of the SSW when the vortex has split and the stratopause vanishes; 13–17 February represent a period during which the stratopause was elevated. Similarly, 9–13 March represent a later time in which the stratopause has dropped but remains elevated compared to climatological values. The central dates of the first two time intervals are depicted in Figures 4a and 4d. The central dates of the latter two time intervals are indicated in Figure 7. Below 50 km, the wind profiles in the two cycles are quantitatively similar. This is also apparent from Figure 6c which shows instantaneous differences of zonal mean winds at 60°N. Between 55 and 70 km, the wind profiles are qualitatively similar. Differences are largest above 75 km. Before the SSW, a typical winter time zonal wind profile is seen (solid curves) with a westerly jet peaking around 35 km. During the SSW (dotted curves), the jet reverses direction becoming easterly with a peak near 40 km. After the SSW when the stratopause
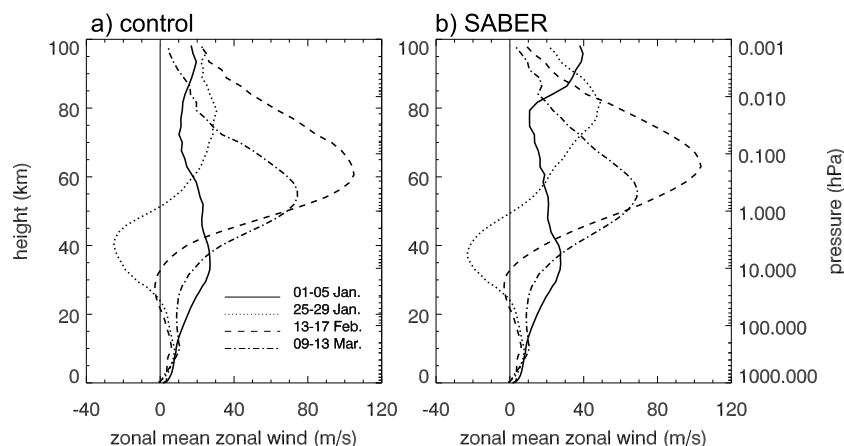

Figure 8. Vertical profile of zonal mean zonal wind at 60°N averaged over 5 day periods (or 17 snapshots) in 2006 for (a) the CONTROL and (b) the SABER assimilation cycles.
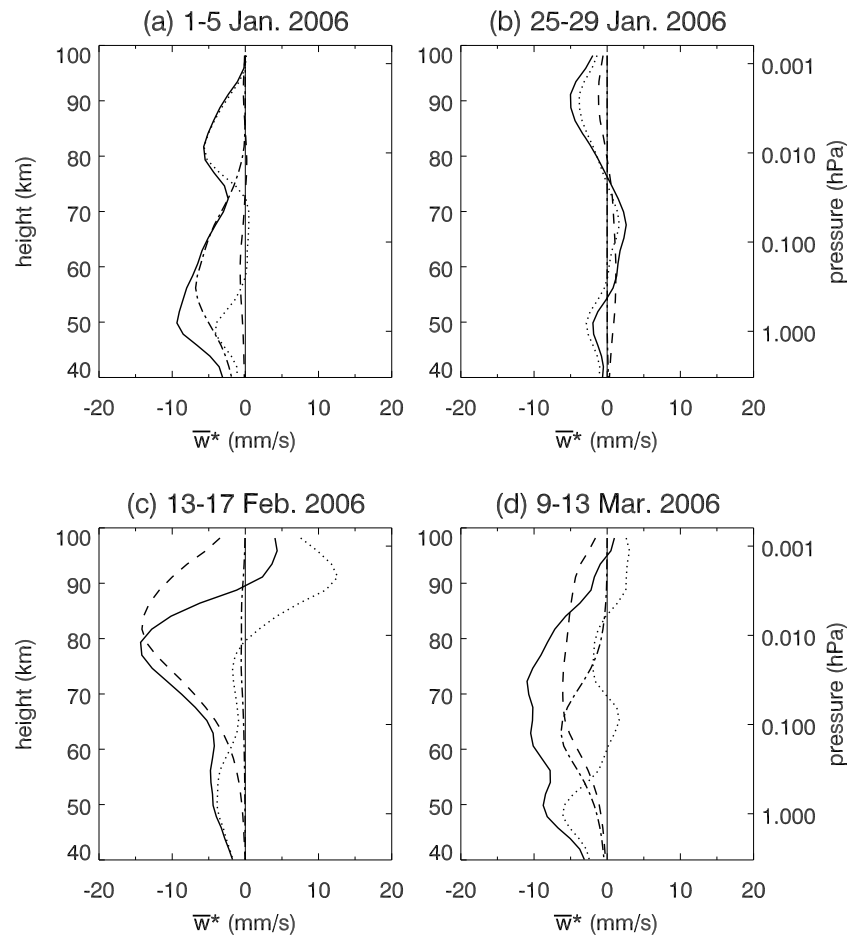
Figure 9. Residual vertical velocity due to wave forcing over the polar cap (60°–90°N) averaged over 5 day periods for the CONTROL assimilation cycle. Total (solid lines), resolved (dotted lines), non-orographic gravity wave drag (GWD) (dashed lines), and orographic GWD (dash-dotted lines) contributions are plotted.

has reformed above 75 km, strong westerlies appear with a jet maximum of 100 m/s at 60 km (dashed curves). As the stratopause descends, the jet maximum decreases to 70 m/s and drops to around 50 km (dash-dotted curves).

[23] The dramatic changes in zonal wind seen in Figure 8 have implications on the filtering of waves whether resolved or parameterized. An analysis of the roles of resolved and parameterized gravity waves during the various stages of the 2006 SSW and the elevated stratopause events was already presented by *Siskind et al.* [2010]. Thus Figure 9 which shows the residual vertical velocity ($\overline{w}*$) due to resolved or parameterized (orographic and nonorographic) gravity waves is used to demonstrate that the CONTROL cycle captures the wave dynamics of this event without the benefit of mesospheric observations. (The residual vertical velocity values from *Ren et al.* [2008, Figure 4b] are too small by a factor of about 7.5 owing to a coding error.) Specifically, Figure 9 is consistent with the analysis of *Siskind et al.* [2010] in the following ways: (1) the role of orographic GWD is seen to be negligible during the peak of the SSW (Figure 9b) and during early February (Figure 9c) because a critical level (zero wind) appears (Figure 8a, dotted curve), filtering the stationary orographically generated waves; (2) nonorographic GWD is seen to be important during the SSW and when the

elevated stratopause has formed (Figures 9c and 9d); and (3) resolved waves contribute to an upwelling near 90 km (Figure 9c). Though the upwelling might be indicative of local planetary wave generation by zonally asymmetric GWD forcing (the *Smith* [1996] mechanism), *Siskind et al.* [2010] showed that nonorographic GWD did not affect the planetary wave amplitude suggesting instead that these waves originated at lower altitudes. (4) In early March when the stratopause has descended somewhat orographic gravity waves contribute to the downwelling below 70 km (Figure 9d) but above 70 km, the downwelling is due to nonorographic GWD. Increased gravity wave activity at 70–90 km was observed by *Hoffmann et al.* [2007] during February and March 2006 in radar data. They also noted that the enhanced gravity wave activity coincided with reduced planetary wave activity. Thus Figures 9c and 9d are consistent with these observations.

[24] Figure 10 is comparable to Figures 9b and 9c but for the SABER cycle. The biggest differences were seen during the peak of the SSW (compare Figures 9b and 10a). The forcing due to nonorographic GWD is double that in the CONTROL cycle while that due to resolved waves is slightly larger. The total downwelling increased by about 50%. This difference can be related to the zonal wind difference. The SABER cycle has an eastward jet maximum of
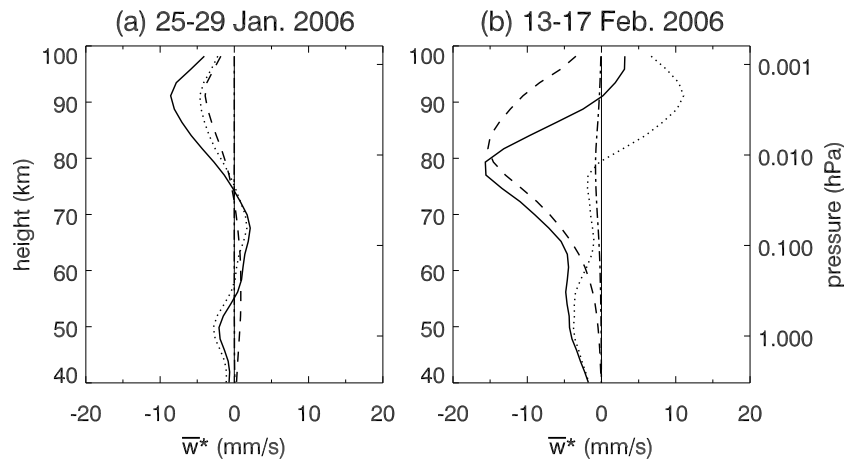
Figure 10. Residual vertical velocity due to wave forcing over the polar cap (60°–90°N) averaged over (a) 25–29 January and (b) 13–17 February 2006 for the SABER cycle. Total (solid lines), resolved (dotted lines), nonorographic GWD (dashed lines), and orographic GWD (dash-dotted lines) contributions are plotted.

50 m/s at 80 km (Figure 8b, dotted curve) while a 30 m/s value is seen in the CONTROL (Figure 8a, dotted curve). With more filtering of eastward gravity waves above 60 km, more westward forcing (and downwelling) is possible. The assimilation of SABER temperatures impacts the zonal wind field in the mesosphere which affects the filtering of waves and thus the residual vertical velocity.

[25] The similarity of the residual vertical velocity plots for the CONTROL and SABER cycles for the periods shown in Figures 9a and 9d (not shown) and Figure 9c can be expected based on the similarity of the zonal wind profiles seen in Figure 8. Because of the quantitative agreement of the wind fields below 50 km, critical level filtering would be the same in both assimilation cycles. The jet structures are generally alike though there is a different maximum value on 9–13 March (dash-dotted curves). For similar jet maxima, the spectrum of waves which are not filtered before reaching the mesosphere would be similar. Then, the drag created through their nonlinear saturation could be replicated if the instantaneous upper mesospheric jet structures are similar (since the drag depends nonlinearly on the difference in wave phase speed relative to launch height and wind speed). (Note that instantaneous zonal mean wind profiles were found to be close below about 50 km but above 75 km profiles were noisier and more dissimilar in the two cycles (not shown).) Thus differences in residual vertical velocity between the CONTROL and SABER cycles are largest above 75 km.

[26] We have shown that the residual vertical velocity in the CONTROL cycle is similar to that of the SABER cycle with the largest differences occurring during the peak of the SSW due to differences in the flow above 75 km. However, both cycles produce less downwelling than the simulations of *Siskind et al.* [2010] who obtain values of −2.5 cm/s for 25–30 January, a period similar (but not identical) to that shown in Figures 9b and 10a. During this time period the vortex has broken down. Later, starting in early February when the vortex has reformed in the upper stratosphere and lower mesosphere, *Manney et al.* [2009b] note that MLS CO starts to descend from the mesosphere and spreads through-

out the vortex by the end of March. Thus the appearance of larger downwelling in Figures 9c and 10b during mid-February are consistent with these observations. Also, the overall magnitudes in Figures 9 and 10 are consistent with the observed long-term descent rate of NO_x of roughly 6 mm/s (inferred by *Randall et al.* [2006, Figure 1]). Although we noted earlier that the calculation of residual vertical velocity was not expected to be realistic because of the steady state assumption made, there are various reasons that our values could differ from those of other models: (1) the CMAM nonzonal sponge layer begins at 80 km so the flow (and thus wave filtering and breaking) should not be considered reliable above these heights, (2) our nonorographic GWD scheme may be producing insufficient forcing, (3) the lack of balanced wind increments in the mesosphere may have reduced the impact of SABER observations, and (4) *Manney et al.* [2009a, 2009b] note that temperature biases, if present, can lead to errors in diabatic descent rates. The most important reason that downwelling could be underestimated is expected to be the lack of an upper atmosphere and the related damping of the flow above 80 km.

[27] In this section we have shown that the CMAM-DAS CONTROL assimilation cycle (in which no observations above 45 km were assimilated) produces realistic simulation of the 2006 SW and the evolution of the stratopause during February and March 2006. General features of winds and temperatures above 45 are well depicted although the flow above 75 km can differ from the SABER cycle leading to differences in residual vertical velocity during the peak of the SSW. Because the nonorographic GWD forcing becomes important above 45 km, the importance of having realistic parameterized drag in a data assimilation cycle is explored in the next section.

4. Impact of GWD on Stratopause Height Evolution

[28] Since nonorographic GWD was shown to be important for the simulation of the elevated stratopause in the last section, we now consider the sensitivity of the analyses in
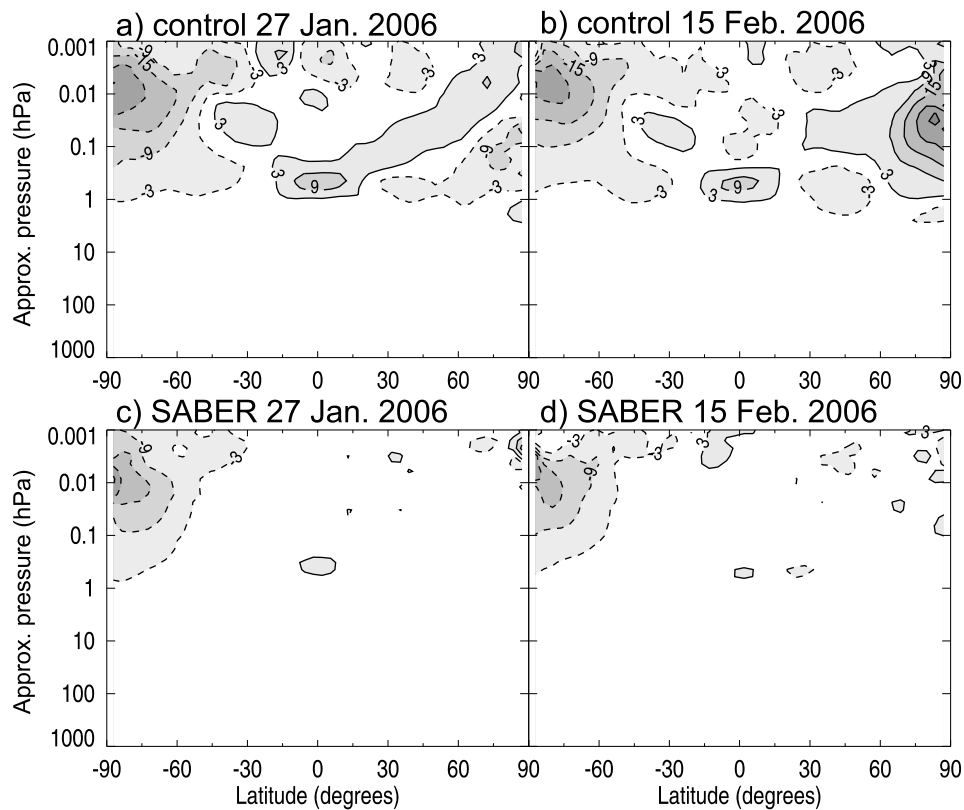
Figure 11. Zonal mean temperature difference due to nonorographic GWD. The difference between CONTROL cycles with and without GWD is shown for (a) 0000 UTC on 27 January 2006 and (b) 0000 UTC on 15 February 2006, while (c, d) the difference between SABER cycles with and without GWD for the same dates are also shown. The contour interval is 6 K, with negative contours dashed.

the upper stratosphere and lower mesosphere to the presence or absence of nonorographic GWD.

[29] In Figure 11, the zonal mean temperature obtained in the CONTROL assimilation cycle is compared with that obtained in an identical cycle except that no nonorographic GWD parameterization was used (CONTROL–no GWD). The impact of nonorographic GWD is restricted to heights above 1 hPa for two reasons. First, observations constrain simulations below 1 hPa whether or not nonorographic GWD is present. Second, wave amplitudes increase as density decreases so nonlinear saturation occurs only when density is low enough. In Figure 11a, at the peak of the SSW, the impact of the nonorographic GWD scheme is maximized at the summer (southern) pole. In the winter hemisphere, the wind profile at that time (Figure 8, dotted curves) filters both westward and eastward traveling gravity waves almost equally so that no net forcing occurs at 60°N. However, when the stratopause is elevated in mid-February (Figure 11b), the presence of nonorographic GWD is important in the CONTROL cycle. At this time, a strong eastward jet is present (Figure 8, dashed curves), preferentially filtering eastward propagating gravity waves so that a net westward force is generated. Thus the importance of having nonorographic GWD depends on the flow configuration. On the other hand, when SABER temperatures are assimilated (Figures 11c and 11d), the impact of nonorographic GWD is diminished everywhere except where there are no SABER observations

(south of 52°S), regardless of the dynamic situation. Thus the assimilation of SABER temperatures has reduced the need for a realistic nonorographic GWD scheme in the CMAM-DAS. Conversely, without mesospheric observations, it is important for data assimilation systems to have a realistic depiction of nonorographic GWD for realistic mesospheric analyses.

[30] Though SABER observations are of temperature, the other dynamic fields are informed through the 6 h model forecasts which are run as part of the assimilation cycle. Figure 12 depicts the impact of nonorographic GWD on the zonal wind field of the CONTROL and SABER cycles. The same conclusions arise here as from Figure 11: with no mesospheric observations, the nonorographic GWD scheme is important when the stratopause is elevated (Figure 12b) but less so during the peak of the SSW (Figure 12a). However, when mesospheric temperatures are assimilated, the impact of the GWD is diminished in the northern middle to high latitudes regardless of the flow configuration. However, now the GWD scheme is seen to have impact in the tropics between 1 and 0.1 hPa. This is because in the tropics, without a clear balance relationship, the mass and wind fields are decoupled so that temperature observations do not greatly influence the wind fields. Thus, even with the assimilation of mesospheric temperature observations, a gap in the observing system is apparent due to the lack of tropical wind observations in the middle atmosphere.
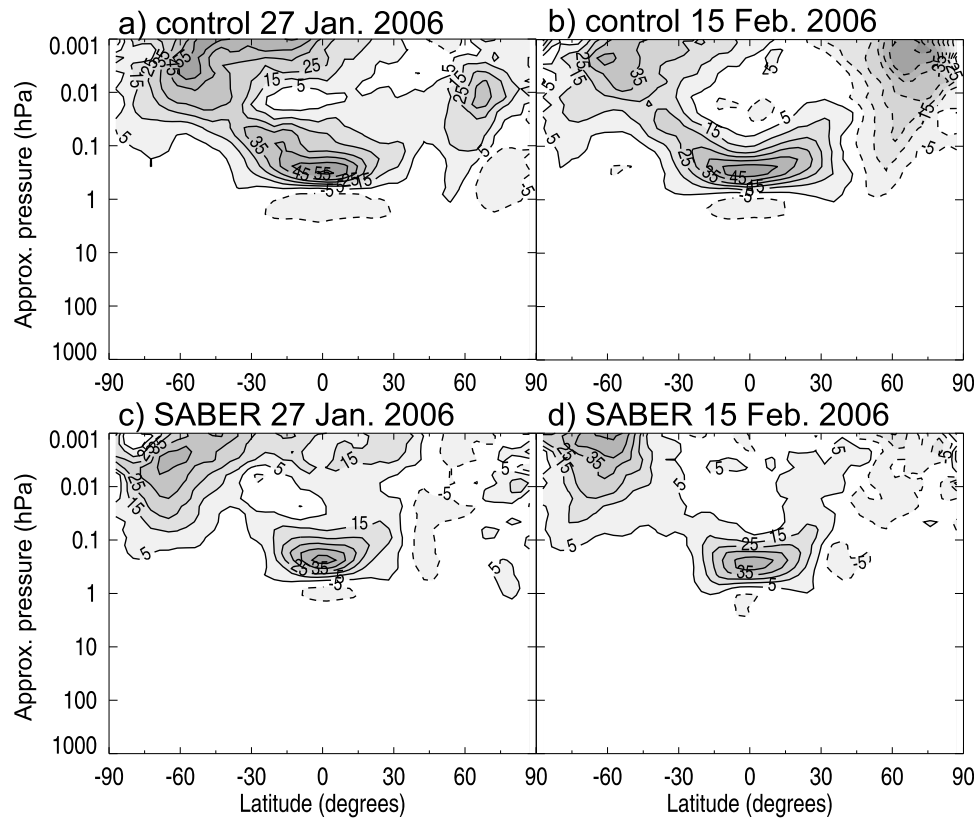
Figure 12. Same as Figure 11, but for zonal mean zonal wind (m/s). The contour interval is 10 m/s, with negative contours dashed.

[31] Figures 11 and 12 show that nonorographic GWD impacts mesospheric analyses when no mesospheric observations are assimilated. However, they do not indicate whether the impact is positive or not. To determine this, we take the SABER assimilation cycle as the reference (or truth) and compute the difference between the CONTROL cycle and the reference. The zonal mean temperature error is shown in Figures 13a and 13b. When nonorographic GWD is present, the mesospheric analyses of the CONTROL cycle are close to those of the SABER cycle. The biggest departures are over the north polar cap during the peak of the SSW (Figure 13a). However, when no nonorographic GWD scheme is used, the error is considerably larger (Figures 13c and 13d). The GWD scheme is having an impact in the southern (summer) polar region, the tropics and in the northern polar region. The error is much larger when no GWD scheme is used, indicating that the GWD scheme is having a beneficial impact on mesospheric analyses, bringing them closer to independent (since SABER was not assimilated in the CONTROL cycles) observations.

[32] Figure 14 compares the zonal wind error of the CONTROL cycles with (Figures 14a and 14b) and without (Figures 14c and 14d) nonorographic GWD to the SABER cycle. As with the temperature field, the zonal wind field is greatly improved if parameterized GWD is used.

[33] In Figures 13 and 14, analyses from the SABER cycle were taken as the "truth." To avoid this assumption, direct comparisons of 6 h forecasts (really 3–9 h forecasts) can be made with SABER observations. Figure 15 demon-strates that the bias and standard deviation of observation minus forecast differences above 45 km are improved when nonorographic GWD is used. In the CONTROL (solid lines) and CONTROL–no GWD (dashed lines), the improvement in standard deviation reaches 5 K at 0.01 hPa and nearly 5 K for bias just below this level. Even when SABER observations are assimilated, using nonorographic GWD is helpful since a consistent improvement in bias and standard deviation is seen above 45 km. The improvement in standard deviation reaches 1 K at 80 km.

[34] In concert with the descent of the stratopause during February and March 2006, a descent of mesospheric constituents was also seen. *Randall et al.* [2006] documented a descent of NO_x = NO + NO_2 and CO from ACE measurements while *Orsolini et al.* [2010] showed descent of H_2O from ODIN-SMR measurements and *Manney et al.* [2009b] saw descent of CO and H_2O from MLS and ACE. Since nonorographic GWD was shown to have a beneficial impact on mesospheric analyses, it is plausible that it also has a positive impact on the depiction of mesospheric constituents. Figures 16a and 16b compares zonal mean NO_x for 30–90°N from CONTROL and CONTROL–no GWD. Figures 16c and 16d shows the same comparison but for SABER and SABER–no GWD. (Recall that no constituent observations were assimilated. The initial conditions for constituents were obtained from a free-running transient CMAM integration for 1990–2005 which was subsequently used to spin up a data assimilation cycle for 1 October to 1 December 2005.) Note that the vertical NO_x distributions
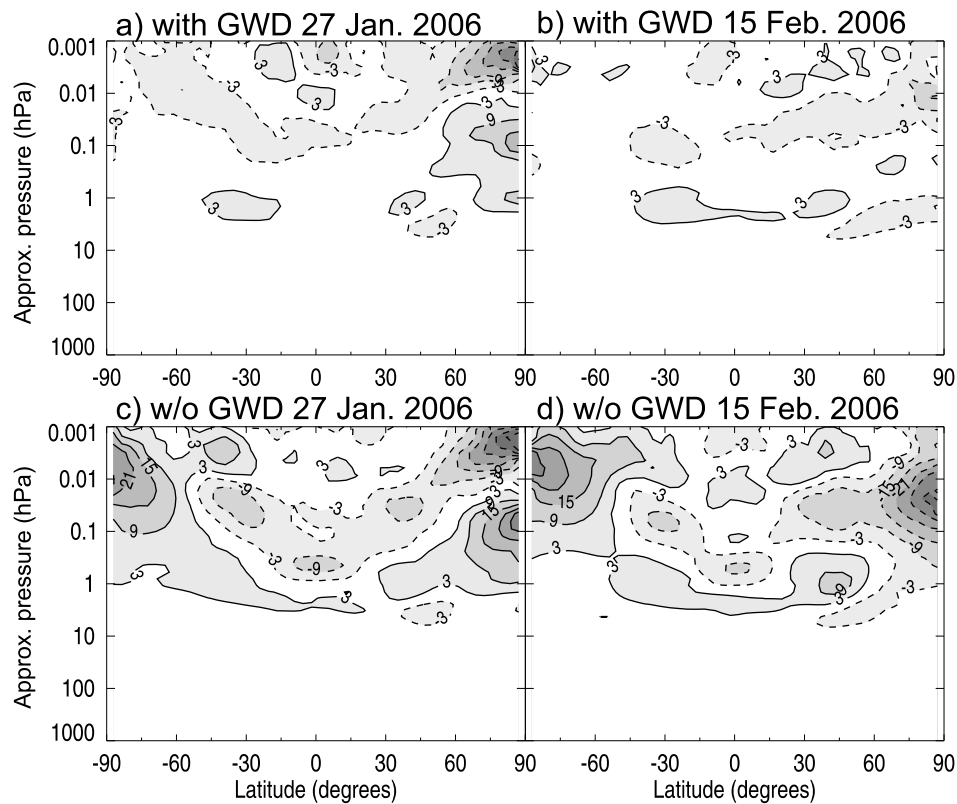
Figure 13. Zonal mean temperature error for the CONTROL cycles (relative to the SABER cycle) (top) with and (bottom) without nonorographic GWD for (a, c) 0000 UTC on 27 January 2006 and (b, d) 0000 UTC on 15 February 2006. The contour interval is 6 K.
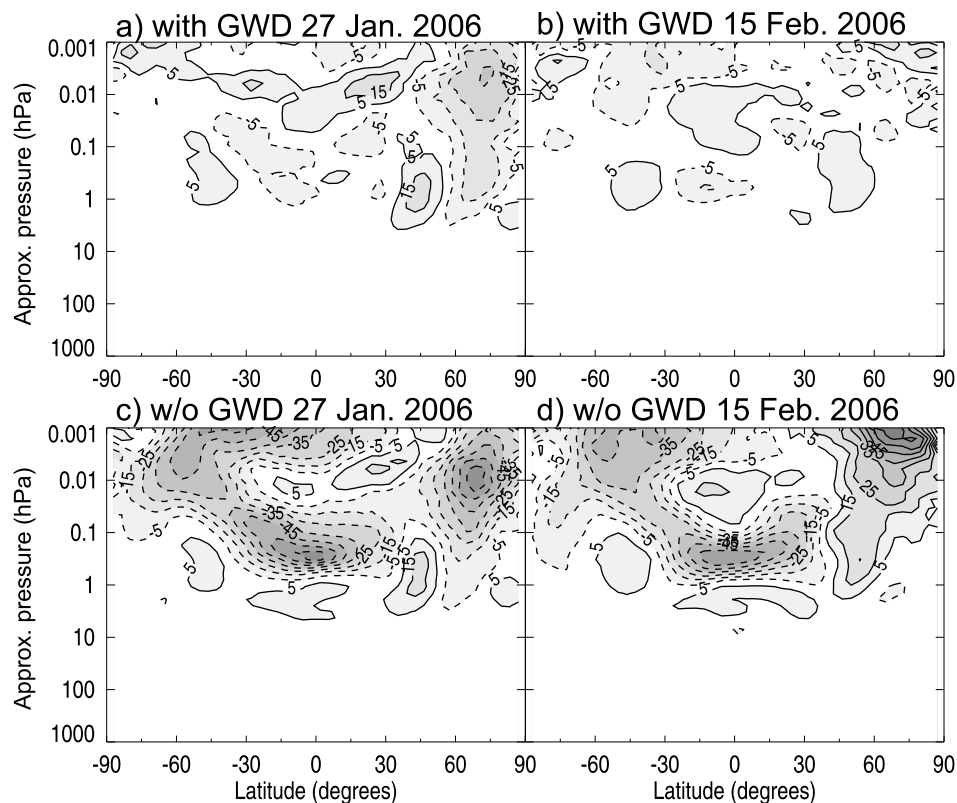

Figure 14. Same as Figure 13, but for zonal mean zonal wind. The contour interval is 10 m/s.
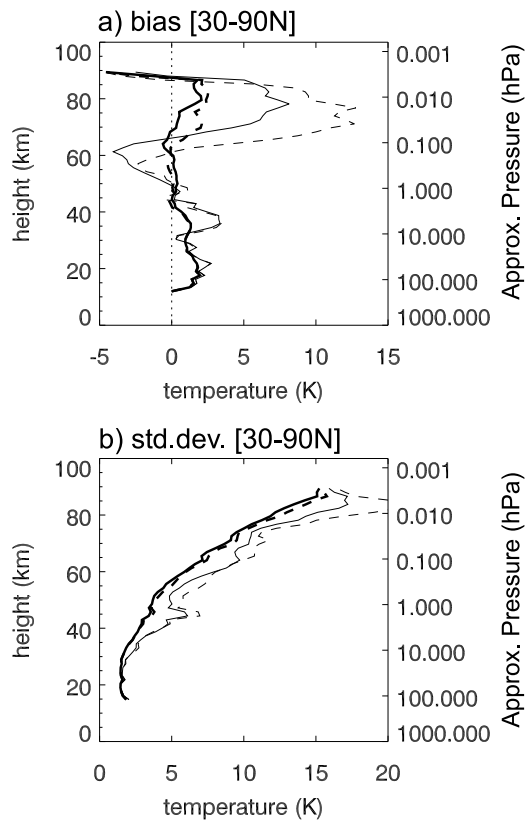
Figure 15. SABER minus 6 h forecast temperatures averaged over 30°–90°N. Statistics were computed for 1–14 February 2006 using 55 samples. (a) Bias and (b) standard deviations are shown. Curves are for the experiments: SABER (bold), SABER–no GWD (bold dashed), CONTROL (solid), CONTROL–no GWD (dashed).

of the CONTROL and SABER cycles differ since the assimilation of temperatures in the SABER cycle impacts reaction rates as well as the overall flow pattern and therefore constituent distributions. This difference accumulates in time over the two months since the start of the assimilation cycles, significantly altering the NO_x background state prior to the sudden warming event.

[35] The main impact of nonorographic GWD on the NO_x distribution is seen in polar latitudes where enhanced descent is obtained with nonorographic GWD (compare Figures 16a and 16b) between 0.1 and 0.01 hPa. This is consistent with Figure 9c which shows that nonorographic GWD contributes strongly to the descent at these levels. Thus, without nonorographic GWD, an important contribution to the meridional circulation and hence the downward transport of NO_x is missing. (The additional transport is a response to the GWD forcing only, as the nonorographic GWD scheme does not include explicit tracer diffusion induced as a result of the wave breaking and turbulence.) When SABER temperatures are assimilated (Figure 16d), a similar impact is seen, that is, in mid-February, more descent of NO_x is seen at polar latitudes with nonorographic GWD. This is consistent with Figures 10a and 10b which shows the importance of nonorographic GWD to descent in the SABER cycle. Although the impact of nonorographic GWD on zonal mean tempera-

ture and wind fields north of 60°N (Figures 11d and 12d) was shown to be smaller when SABER temperatures were assimilated, suggesting the new observations have helped correct the flow structure, the downwelling over the winter pole occurs through downward control [*Haynes et al.*, 1991] which also involves eddy forcing terms. Thus the assimilation of SABER observations helps to define the zonal mean fields and the resolved wave state, but the descent of NO_x (and other constituents) also depends on the accurate representation of the total eddy forcing. From Figure 3, we expect that the CONTROL cycle does not well constrain wave numbers higher than 10 when SABER temperatures are assimilated, thus eddy forcing is not expected to be fully constrained. Therefore, the nonorographic GWD parameterization, which provides a representation of the subgrid waves and their impact may still be relevant for mesospheric data assimilation systems even when mesospheric temperatures are assimilated. Thus we conclude that for realistic depiction of mesospheric constituents, it is also important to realistically simulate nonorographic GWD. Furthermore, we postulate that observations of mesospheric constituents contain information on transport that could be exploited to help constrain GWD parameters or sources.

5. Summary and Conclusions

[36] In this work, we have shown that the CMAM-DAS can simulate the 2006 SSW and elevated stratopause event even without assimilating any mesospheric observations. The main features of the flow above 45 km were shown to be realistic by comparing to an assimilation cycle which assimilated SABER temperatures. Specifically, the timing of the stratopause disappearance in late January and its subsequent reappearance above 75 km were captured. The quality of mesospheric analyses obtained without assimilating mesospheric observations is attributed to the use of a nonorographic GWD. While *Siskind et al.* [2010] showed that nonorographic GWD is important for simulating stratopause evolution during February and March 2006 and for capturing the descent of mesospheric constituents in the context of forecasts, here we demonstrate the importance of realistically depicting GWD in a data assimilation cycle. This makes sense because the fundamental processes of critical level filtering, propagation and nonlinear saturation of gravity waves are being simulated by these schemes. Observations in the troposphere and stratosphere constrain the winds below 45 km so that the critical level filtering process is well depicted. So long as the jet maximum and its location are captured, the spectrum of waves that reach the mesosphere and exert a drag is realistic. However, details of the mesospheric wind field will impact the amount of drag deposited due to nonlinear saturation since the drag is a nonlinear function of the departure of the wave phase speed and wind speeds.

[37] The assimilation of mesospheric temperatures reduced the sensitivity of mesospheric analyses of wind and temperature to the presence of a nonorographic GWD scheme. Thus, the assimilation of SABER temperatures has reduced the importance of having a realistic nonorographic GWD scheme in CMAM. Conversely, without mesospheric observations, it is important for data assimilation systems to have
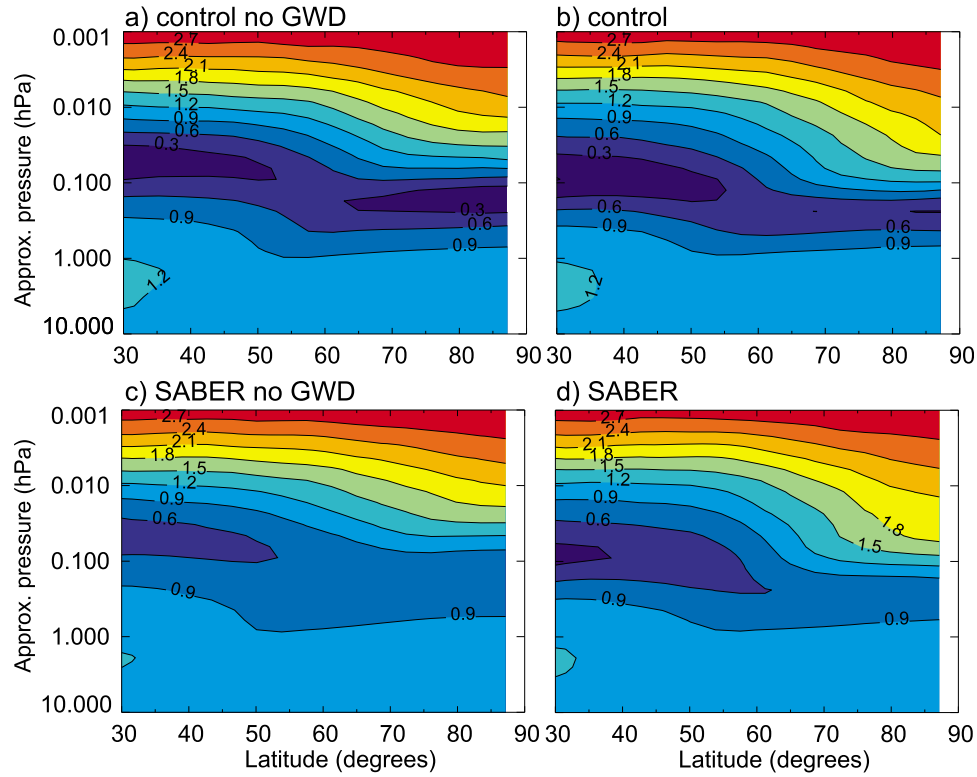
Figure 16. Height-latitude sections of $\log_{10}$ of zonal mean NO_x (ppbv) with and without nonorographic GWD in the Northern Hemisphere. The analyzed NO_x field obtained (a, c) with and (b, d) without GWD is shown for 0000 UTC on 15 February 2006 for (top) the CONTROL cycles and (bottom) the SABER cycles. The contour interval is 0.3.

a realistic depiction of nonorographic GWD for realistic mesospheric analyses.

[38] SABER temperature assimilation has a greater impact on the evolution of polar wind and temperatures during the peak of the SSW when the polar vortex breaks down and the stratopause disappears than during the elevated stratopause event. This suggests that mesospheric observations may be particularly valuable during highly dynamic situations. On the other hand, due to the lack of a mass-wind balance in the tropics, SABER temperature assimilation did not improve wind analyses in the tropical middle atmosphere.

[39] Since nonorographic GWD is able to bring simulations closer to the observations, this suggests that mesospheric observations contain information which can be used to constrain GWD parameters (as in the work of *Pulido et al.* [2011]) or properties of GW sources. However, the impact of nonorographic GWD depends on flow situation so not all atmospheric states are equally useful for parameter estimations. The assimilation of SABER primarily informs large scales in the mesosphere (below wave number 10) and the stratosphere (below wave number 30) (in the ideal case where neither the model nor observations have bias). If this result holds in realistic cases and for other systems, then it is the large scales in the mesosphere that contain useful information for constraining GWD.

[40] The depiction of the descent of mesospheric NO_x was found to be sensitive to the use of a nonorographic GWD scheme. This sensitivity was present whether or not mesospheric temperatures were assimilated. Since the residual

vertical velocity depends not only on zonal mean fields but also on eddy forcing, this result suggests that the assimilation of mesospheric temperatures in the CMAM-DAS did not constrain the eddy forcing due to synoptic or smaller scales. This then implies that for realistic depictions of mesospheric constituents it is still necessary to simulate nonorographic GWD even if mesospheric observations are assimilated and that the constituent distributions can provide useful information on constraining the GWD parameterization configuration used in models. Furthermore, since different constituents will highlight different aspects of the mesospheric analysis (on various geographic and spatial scales), the assessment of multiple chemical tracers can provide additional degrees of freedom with which to evaluate the model state and the success of the assimilation system.

Appendix A: Calculation of Residual Vertical Velocity

[41] We compute $\overline{w}^*$ following *Haynes et al.* [1991, equation (2.7)] but integrate over pressure instead of height:

$$\overline{w}^* = \frac{1}{\rho_o a \cos\varphi} \frac{\partial}{\partial\varphi} \int_P^0 \frac{\Im \cos\varphi}{fg} \, dp. \tag{A1}$$

[42] Here $\Im$ is zonal wind forcing (in ms^{-2}) due to wave drag from resolved waves or parameterized gravity waves,

ϕ is latitude, p is pressure, g is gravitational acceleration, f is the Coriolis parameter and ρ_o is an exponential density profile using a scale height of 7 km and a is the Earth's radius. In Figure 9, $\overline{w}^*$ is area weighted over the polar cap (60°–90°N) and averaged over 17 snapshots. For resolved waves, $\Im$ is computed from the Eliassen-Palm flux divergence. For parameterized waves $\Im$ is obtained from the drag components computed by the GWD schemes.

References

Alexander, M. J., et al. (2010), Recent developments in gravity-wave effects in climate models and the global distribution of gravity-wave momentum flux from observations and models, *Q. J. R. Meteorol. Soc.*, 136, 1103–1124, doi:10.1002/qj.637.

Andrews, D. G., J. R. Holton, and C. B. Leovy (1987), *Middle Atmosphere Dynamics*, Academic, Orlando, Fla.

Bernath, P. F., et al. (2005), Atmospheric Chemistry Experiment (ACE): Mission overview, *Geophys. Res. Lett.*, 32, L15S01, doi:10.1029/2005GL022386.

Bloom, S. C., L. L. Takacs, A. M. DaSilva, and D. Ledvina (1996), Data assimilation using incremental analysis updates, *Mon. Weather Rev.*, 124, 1256–1271, doi:10.1175/1520-0493(1996)124<1256:DAUIAU>2.0.CO;2.

Boer, G. J. (1995), A hybrid moisture variable suitable for spectral GCMs, *Res. Activ. in Atmos. and Oceanic Modell. Rep. 21, WMO/TD 665*, World Meteorol. Organ., Geneva, Switzerland.

Buehner, M. (2005), Ensemble-derived stationary and flow-dependent background-error covariances: Evaluation in a quasi-operational NWP setting, *Q. J. R. Meteorol. Soc.*, 131, 1013–1043, doi:10.1256/qj.04.15.

Coy, L., S. Eckermann, and K. Hoppel (2009), Planetary wave breaking and tropospheric forcing as seen in the stratospheric sudden warming of 2006, *J. Atmos. Sci.*, 66, 495–507, doi:10.1175/2008JAS2784.1.

de Grandpré, J., S. R. Beagley, V. I. Fomichev, E. Griffioen, J. C. McConnell, A. S. Medvedev, and T. G. Shepherd (2000), Ozone climatology using interactive chemistry: Results from the Canadian Middle Atmosphere Model, *J. Geophys. Res.*, 105, 26,475–26,491, doi:10.1029/2000JD900427.

Eyring, V., T. G. Shepherd, and D. W. Waugh (Eds.) (2010), Stratospheric processes and their role in climate: SPARC report on the evaluation of chemistry-climate models, *SPARC Rep. 5*, SPARC, World Meteorol. Organ., Geneva, Switzerland.

Hauchecorne, A., J. L. Bertaux, F. Dalaudier, J. M. Russell III, M. G. Mlynczak, E. Kyrölä, and D. Fussen (2007), Large increase of NO$_2$ in the north polar mesosphere in January–February 2004: Evidence of a dynamical origin from GOMOS/ENVISAT and SABER/TIMED data, *Geophys. Res. Lett.*, 34, L03810, doi:10.1029/2006GL027628.

Haynes, P. H., M. E. McIntyre, T. G. Shepherd, C. J. Marks, and K. P. Shine (1991), On the "downward control" of extratropical diabatic circulations by eddy-induced mean zonal forces, *J. Atmos. Sci.*, 48, 651–678, doi:10.1175/1520-0469(1991)048<0651:OTCOED>2.0.CO;2.

Hoffmann, P., W. Singer, D. Keuer, W. K. Hocking, M. Kunze, and Y. Murayama (2007), Latitudinal and longitudinal variability of mesospheric winds and temperatures during stratospheric warming events, *J. Atmos. Sol. Terr. Phys.*, 69, 2355–2366, doi:10.1016/j.jastp.2007.06.010.

Hoppel, K. W., N. L. Baker, L. Coy, S. D. Eckermann, J. P. McCormack, G. E. Nedoluha, and D. E. Siskind (2008), Assimilation of stratospheric and mesospheric temperatures from MLS and SABER into a global NWP model, *Atmos. Chem. Phys.*, 8, 6103–6116, doi:10.5194/acp-8-6103-2008.

Jackson, D. R., M. Keil, and B. J. Devenish (2008), Use of Canadian Quick covariances in the Met Office data assimilation system, *Q. J. R. Meteorol. Soc.*, 134, 1567–1582, doi:10.1002/qj.294.

Koshyk, J., B. Boville, K. Hamilton, E. Manzini, and K. Shibata (1999), Kinetic energy spectrum of horizontal motions in middle-atmosphere models, *J. Geophys. Res.*, 104, 27,177–27,190, doi:10.1029/1999JD900814.

Labitzke, K. (1972), Temperature changes in the mesosphere and stratosphere connected with circulation changes in winter, *J. Atmos. Sci.*, 29, 756–766, doi:10.1175/1520-0469(1972)029<0756:TCITMA>2.0.CO;2.

Limpasuvan, V., J. H. Richter, Y. J. Orsolini, F. Stordal, and O.-K. Kvissel (2011), The roles of planetary and gravity waves during a major stratospheric sudden warming as characterized in WACCM, *J. Atmos. Sol. Terr. Phys.*, doi:10.1016/j.jastp.2011.03.004, in press.

Manney, G. L., et al. (2008), The evolution of the stratopause during the 2006 major warming: Satellite data and assimilated meteorological analyses, *J. Geophys. Res.*, 113, D11115, doi:10.1029/2007JD009097.

Manney, G. L., M. J. Schwartz, K. Kruger, M. L. Santee, S. Pawson, J. N. Lee, W. H. Daffer, R. A. Fuller, and N. J. Livesey (2009a), Aura Microwave Limb Sounder observations of dynamics and transport during the record-breaking 2009 Arctic stratospheric major warming, *Geophys. Res. Lett.*, 36, L12815, doi:10.1029/2009GL038586.

Manney, G. L., et al. (2009b), Satellite observations and modeling of transport in the upper troposphere through the lower mesosphere during the 2006 major stratospheric sudden warming, *Atmos. Chem. Phys.*, 9, 4775–4795, doi:10.5194/acp-9-4775-2009.

Matsuno, T. (1971), A dynamical model of the stratospheric sudden warming, *J. Atmos. Sci.*, 28, 1479–1494, doi:10.1175/1520-0469(1971)028<1479:ADMOTS>2.0.CO;2.

Murtagh, D., et al. (2002), An overview of the Odin atmospheric mission, *Can. J. Phys.*, 80, 309–319, doi:10.1139/p01-157.

Nezlin, Y., Y. J. Rochon, and S. Polavarapu (2009a), Impact of tropospheric and stratospheric data assimilation on mesospheric prediction, *Tellus, Ser. A*, 61, 154–159, doi:10.1111/j.1600-0870.2008.00368.x.

Nezlin, Y., S. Polavarapu, and Y. J. Rochon (2009b), A new method of assessing filtering schemes in data assimilation systems, *Q. J. R. Meteorol. Soc.*, 135, 1059–1070, doi:10.1002/qj.418.

Orsolini, Y. J., J. Urban, D. P. Murtagh, S. Lossow, and V. Limpasuvan (2010), Descent from the polar mesosphere and anomalously high stratopause observed in 8 years of water vapor and temperature satellite observations by the Odin sub millimeter radiometer, *J. Geophys. Res.*, 115, D12305, doi:10.1029/2009JD013501.

Polavarapu, S., S. Ren, A. M. Clayton, D. Sankey, and Y. J. Rochon (2004), On the relationship between incremental analysis updating and incremental digital filtering, *Mon. Weather Rev.*, 132, 2495–2502, doi:10.1175/1520-0493(2004)132<2495:OTRBIA>2.0.CO;2.

Polavarapu, S., S. Ren, Y. Rochon, D. Sankey, N. Ek, J. Koshyk, and D. Tarasick (2005), Data assimilation with the Canadian Middle Atmosphere Model, *Atmos. Ocean*, 43, 77–100, doi:10.3137/ao.430105.

Polavarapu, S., E. Farahani, G. Manney, and T. G. Shepherd (2008), Report on the joint SPARC workshop on data assimilation and International Polar Year (IPY), *SPARC Newsl.*, 30, 27–33.

Pulido, M., S. Polavarapu, T. G. Shepherd, and J. Thuburn (2011), Estimation of optimal gravity wave parameters for climate models using a genetic algorithm, *Q. J. R. Meteorol. Soc.*, doi:10.1002/qj.932, in press.

Randall, C. E., V. L. Harvey, C. S. Singleton, P. F. Bernath, C. D. Boone, and J. U. Kozyra (2006), Enhanced NO$_x$ in 2006 linked to strong upper stratospheric Arctic vortex, *Geophys. Res. Lett.*, 33, L18811, doi:10.1029/2006GL027160.

Remsberg, E. E., et al. (2008), Assessment of the quality of the version 1.07 temperature versus pressure profiles of the middle atmosphere from TIMED/SABER, *J. Geophys. Res.*, 113, D17101, doi:10.1029/2008JD010013.

Ren, S., S. Polavarapu, and T. G. Shepherd (2008), Vertical propagation of information in a middle atmosphere data assimilation system by gravity-wave drag feedbacks, *Geophys. Res. Lett.*, 35, L06804, doi:10.1029/2007GL032699.

Russell, J. M., III, M. G. Mlynczak, L. L. Gordley, J. Tansock, and R. Esplin (1999), An overview of the SABER experiment and preliminary calibration results, *Proc. SPIE*, 3756, 277–288, doi:10.1117/12.366382.

Sankey, D., S. Ren, S. Polavarapu, Y. J. Rochon, Y. Nezlin, and S. Beagley (2007), Impact of data assimilation filtering methods on the mesosphere, *J. Geophys. Res.*, 112, D24104, doi:10.1029/2007JD008885.

Scinocca, J. F., N. A. McFarlane, M. Lazare, and J. Li (2008), The CCCma third generation AGCM and its extension into the middle atmosphere, *Atmos. Chem. Phys.*, 8, 7055–7074, doi:10.5194/acp-8-7055-2008.

Shepherd, T. G. (2008), Dynamics, stratospheric ozone and climate change, *Atmos. Ocean*, 46, 117–138, doi:10.3137/ao.460106.

Simmons, A. (2000), Assimilation of satellite data for numerical weather prediction: Basic importance, concept and issues, in *Exploitation of the New Generation of Satellite Instruments for Numerical Weather Prediction*, pp. 21–46, Eur. Cent. for Medium-Range Weather Forecasts, Reading, U. K.

Siskind, D. E., S. D. Eckermann, L. Coy, J. P. McCormack, and C. E. Randall (2007), On recent interannual variability of the Arctic winter mesosphere: Implications for tracer decent, *Geophys. Res. Lett.*, 34, L09806, doi:10.1029/2007GL029293.

Siskind, D. E., S. D. Eckermann, J. P. McCormack, L. Coy, K. W. Hoppel, and N. L. Baker (2010), Case studies of the mesospheric response to

recent minor, major, and extended stratospheric warmings, *J. Geophys. Res.*, *115*, D00N03, doi:10.1029/2010JD014114.

Smith, A. K. (1996), Longitudinal variations in mesospheric winds: Evidence for gravity wave filtering by planetary waves, *J. Atmos. Sci.*, *53*, 1156–1173, doi:10.1175/1520-0469(1996)053<1156:LVIMWE>2.0. CO;2.

Thurairajah, B., R. L. Collins, V. L. Harvey, R. S. Lieberman, and K. Mizutani (2010), Rayleigh lidar observations of reduced gravity wave activity during the formation of an elevated stratopause in 2004 at Chatanika, Alaska (65°N, 147°W), *J. Geophys. Res.*, *115*, D13109, doi:10.1029/ 2009JD013036.

Waters, J. W., et al. (2006), The Earth Observing System Microwave Limb Sounder (EOS MLS) on the Aura satellite, *IEEE Trans. Geosci. Remote Sens.*, *44*, 1075–1092, doi:10.1109/TGRS.2006.873771.

Wright, C. J., S. M. Osprey, J. J. Barnett, L. J. Gray, and J. C. Gille (2010), High Resolution Dynamics Limb Sounder measurements of gravity wave activity in the 2006 Arctic stratosphere, *J. Geophys. Res.*, *115*, D02105, doi:10.1029/2009JD011858.

S. R. Beagley, Department of Earth and Space Science and Engineering, York University, 4700 Keele St., Toronto, ON M3J 1P3, Canada.

Y. Nezlin and S. Ren, Department of Physics, University of Toronto, 60 St. George St., Toronto, ON M5S 1A7, Canada.

S. Polavarapu and Y. J. Rochon, Environment Canada, 4905 Dufferi St., Toronto, ON M3H 5T4, Canada. (saroja.polavarapu@ec.gc.ca)